# Shape Sensing Based on Longitudinal Strain Measurements Considering Elongation, Bending and Twisting

Vincent Modes, Tobias Ortmaier, and Jessica Burgner-Kahrs, *Senior Member, IEEE*

***Abstract*— The inherent flexibility, the small dimensions as well as the curvilinear shape of continuum robots makes it challenging to precisely measure their shape. Optical fibers with Bragg gratings (FBGs) provide a powerful tool to reconstruct the centerline of continuum robots. We present a theoretical model to determine the shape of such a sensor array based on longitudinal strain measurements and incorporating bending, twisting, and elongation. To validate our approach, we conduct several simulations by calculating arbitrary shapes based on the Cosserat rod theory. Our algorithm showed a maximum mean relative shape deviation of 0.04%, although the sensor array was twisted up to 78°. Because we derive a closed-form solution for the strain curvature twist model, we also give analytical sensitivity values for the model, which can be used in the calculation of error propagation.**

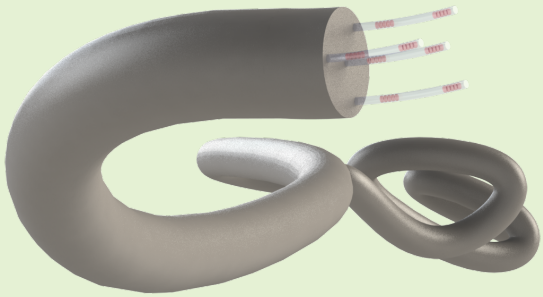

***Index Terms*— continuum robot, fiber Bragg grating sensors, multi-core optical fiber, shape sensing**

## I. Introduction

### A. Related work

SHAPE sensing of long and (comparable to their length) slender rods has been important in various fields of engineering, such as civil engineering or mechanical engineering. Additional attention in this topic arises with the increasing research effort in the field of continuum robotics. As opposed to conventional serial robots they do not consist of a finite number of rigidly connected joints, but are made of flexible materials [1], [2]. They show an inherent flexibility that allows modeling their shape as a continuous spatial curve. In combination with their small dimensions, they are well suited for minimally invasive surgery [3] or inspection/ maintenance tasks in confined spaces [4]. Nevertheless, these properties make it also challenging to measure their shape precisely [5]. Commonly used measurement systems use imaging technology to reconstruct the shape. However, these require either a direct line of sight to the robot [6] or rely on fluoroscopy [7] which requires elaborate and expensive equipment. Electromagnetic tracking coils integrated into the robot allow measuring the position of distinct points along the robot's centerline [8]. However, the number of coils inserted inside the robot is limited. Guo *et al.* measure the magnetic field of permanent magnets distributed along the robots centerline to reconstruct its shape [9]. Nevertheless, all magnetic sensing systems are not suitable for application environments with ferromagnetic materials present (e.g. inspection tasks in aerospace engines).

A promising technology are optical fibers with inscribed fiber Bragg gratings (FBG). Each grating can be seen as an optical strain gauge. By inscribing several FBGs into one single optical fiber, it is possible to measure strain at various locations along its centerline. Arranging several fibers in a known geometrical configuration creates a sensor array with a high spatial sensor density and small physical dimensions. The sensor array can either consist of several distinct optical fibers or of a single multicore fiber with several fiber cores, each containing various FBGs as depicted in Fig. 1a.

Often, the fibers are arranged in parallel to the centerline of the sensor array which we denote as a *longitudinal* arrangement. With the help of the known geometrical relations of the array's cross-section, the shape of the deformed array can be reconstructed [10], [11], [12]. Various researchers apply this approach to reconstruct the centerline of continuum robots, e.g. [13], [14] or [15]. In contrast to models based on geometric relations, Sefati *et al.* [16] implement a data-driven linear regression model which requires an extensive pre-operative model training. Until now, all presented algorithms require an untwisted sensor array and a twist-free sensor integration must be assured. Furthermore, twisting torques acting on the sensor array/ robot can not be detected without the help of additional sensors. However, there exist a variety of continuum robots,

This work was partly supported by the German Research Foundation under grant number BU 2935/1-1.

Vincent Modes, and Tobias Ortmaier are affiliated with the Institute of Mechatronic Systems, Leibniz University Hannover, Garbsen, Germany (e-mail: vincent.modes@imes.uni-hannover.de).

Jessica Burgner-Kahrs is affiliated with the Department of Mathematical & Computational Sciences, University of Toronto, Canada.

whose actuation inherently causes material twisting [17], [18]. Measuring their shape and material twist simultaneously, can improve accuracy in model-based applications such as closed-loop control.

To achieve this, the optical fibers can be wound helically around the centerline of the sensing array, called a *helical* arrangement. Helical sensor arrays allow simultaneous measurement of the curvature and the twist angle of the array [19], [20]. Lim and Han [21] model the sensor array as a superhelix (i.e. also the centerline of the array follows a helical path) and derive an analytical solution. However, their model is not applicable, if the sensor array is completely straight. Furthermore, manufacturing this type of sensor array requires high precision and is more complex than creating a longitudinal arrangement [22]. If shape and twisting could be calculated with a longitudinal sensor array, simpler robot designs could be realized by simultaneously improving the results of kinematic calculations. Chadha and Todd [23] present a sophisticated beam mechanics model incorporating the effects of elongation as well as warping of the sensor array's cross-section. It shows, that twisting influences the strain measurements even though a longitudinal sensor arrangement is used in the array. However, they only propose a shape reconstruction algorithm, which requires a helical sensor arrangement [24]. Guo *et al.* [25] present a calibration procedure to compensate twist induced in the sensor array during manufacturing. Yet, their method can not compensate for sensor array twisting, which occurs after the calibration. Separating bending and torsion for reconstruction of the shape has just recently been addressed by Yi *et al.* [26]. They use a numerical, non-linear least squares method to calculate twist and bending parameters from the sensor readouts.

Hence, to the best knowledge of the authors, the state-of-the-art lacks an analytical method to simultaneously calculate the shape and twisting of a longitudinal sensor array.

### B. Contribution

The main contribution of this paper is to present a shape reconstruction algorithm based on measurements of strain sensors, which are arranged longitudinally in a sensor array with a circular cross-section. Our approach is not limited to pure bending, but also incorporates twisting and elongation. The longitudinal sensor setup simplifies sensor placement. Deriving closed-form formulas for the curve parameters, we use differential geometry to calculate a three times differentiable curve representing the centerline of the array. Additionally, we provide closed-form equations for sensitivities of curvature, bending direction, and twist rate which can be used to calculate error propagation.

## II. Shape Reconstruction Algorithm

Our approach assumes a sensor array consisting of three outer sensors with index $i \in \{1, 2, 3\}$ and one central sensor coaxial to the centerline $\boldsymbol{\gamma}(s)$ as depicted in Fig. 1a. We model the centerline as a three-dimensional curve using differential geometry. In the remainder of the paper, we assume, that the sensor array is an FBG multicore fiber. To determine the curve

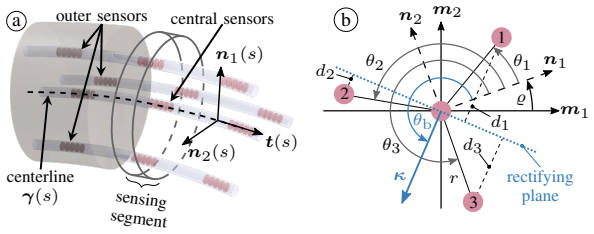


Fig. 1. Multicore FBG fiber used as sensor array: (a) All three outer sensors have the same distance $\boldsymbol{r}$ from the array's centerline $\boldsymbol{\gamma}(\boldsymbol{s})$, while the central sensors are coaxial to $\boldsymbol{\gamma}(\boldsymbol{s})$. The vectors $\boldsymbol{t}(\boldsymbol{s})$, $\boldsymbol{n_1}(\boldsymbol{s})$ and $\boldsymbol{n_2}(\boldsymbol{s})$ form the material frame of the array. (b) Cross-section of sensing segment at arc length $\boldsymbol{s}$. Vectors $\boldsymbol{m_1}, \boldsymbol{m_2}$ and $\boldsymbol{n_1}, \boldsymbol{n_2}$ are part of the untwisted and twisted material frame, respectively. Outer sensors with index $\boldsymbol{i} \in \boldsymbol{\{1, 2, 3\}}$ and central sensor are marked in purple. $\boldsymbol{\theta_i}$ is the angle between sensor $\boldsymbol{i}$ and vector $\boldsymbol{n_1}$. $\boldsymbol{\varrho}$ denotes the twist angle at the current arc length. $\boldsymbol{d_i}$ is the distance from sensor $\boldsymbol{i}$ to the rectifying plane.

parameters, we present a strain curvature twist model that evaluates strain measurements in a cross-section at a specific point along the sensor array. By interpolating the distinct strain measurements along the centerline, curve parameters for the complete length of the array are derived.

### A. Centerline of sensor array

Let $\boldsymbol{\gamma}(s)$ be a spatial curve parameterized by arc length $s$ which represents the sensor array's centerline. Then $\boldsymbol{t}(s)$ is the unit tangent vector of $\boldsymbol{\gamma}(s)$, which implies $\boldsymbol{\gamma}(s) = \int_{s_0}^{s} \boldsymbol{t}(\sigma)\,\mathrm{d}\sigma + \boldsymbol{\gamma}(s_0)$. At every point of $\boldsymbol{\gamma}(s)$, a set of three orthonormal vectors $\boldsymbol{t}(s)$, $\boldsymbol{m}_1(s)$ and $\boldsymbol{m}_2(s)$ is defined, which form a Bishop frame (also referred to as Parallel Transport frame). Bishop showed [27], that, together with the curve's curvature $\kappa(s)$ and bending direction $\theta_\mathrm{b}(s)$, these vectors are related to each other by a set of differential equations: $\boldsymbol{t}'(s) = k_1\boldsymbol{m}_1(s) + k_2\boldsymbol{m}_2(s)$, $\boldsymbol{m}_1'(s) = -k_1\boldsymbol{t}(s)$ and $\boldsymbol{m}_2'(s) = -k_2\boldsymbol{t}(s)$ with $k_1 = \kappa(s)\cos(\theta_\mathrm{b}(s))$ and $k_2 = \kappa(s)\sin(\theta_\mathrm{b}(s))$. The superscript $'$ denotes the derivation w.r.t. arc length $s$. Solving these equations and integrating $\boldsymbol{t}(s)$ yields the centerline of an *unelongated* and *untwisted* sensor array, with $\boldsymbol{t}(s)$, $\boldsymbol{m}_1(s)$ and $\boldsymbol{m}_2(s)$ representing its material frame at $s$. In contrast to the often used Frenet–Serret frames, a Bishop frame is also defined if $\kappa = 0$ and consequently can be used to model a straight centerline.

However, if the array is *twisted*, its material frame $\boldsymbol{t}(s)$, $\boldsymbol{n}_1(s)$, $\boldsymbol{n}_2(s)$ rotates around $\boldsymbol{t}(s)$ such that $\boldsymbol{m}_1(s)$ and $\boldsymbol{n}_1(s)$ enclose an angle $\varrho(s)$ as shown in Fig. 1b. Adapting from [28], this can be expressed by the following set of differential equations

$$\begin{bmatrix} \boldsymbol{\gamma}'(s) \\ \boldsymbol{t}'(s) \\ \boldsymbol{n}_1'(s) \\ \boldsymbol{n}_2'(s) \end{bmatrix} = \begin{bmatrix} 0 & 1+\varepsilon_\mathrm{a} & 0 & 0 \\ 0 & 0 & k_1 & k_2 \\ 0 & -k_1 & 0 & \varrho' \\ 0 & -k_2 & -\varrho' & 0 \end{bmatrix} \begin{bmatrix} \boldsymbol{\gamma}(s) \\ \boldsymbol{t}(s) \\ \boldsymbol{n}_1(s) \\ \boldsymbol{n}_2(s) \end{bmatrix} \tag{1}$$

with $\varepsilon_\mathrm{a}$ the longitudinal strain at the array centerline.

Choosing arbitrary start values for $\boldsymbol{\gamma}(s_0)$, $\boldsymbol{t}(s_0)$, $\boldsymbol{n}_1(s_0)$ and $\boldsymbol{n}_2(s_0)$, (1) can be solved numerically.

### B. Fiber Bragg grating sensors

While the presented algorithm is generally applicable to any longitudinal strain sensor, optical fibers with fiber Bragg gratings (FBGs) are commonly used as such sensors. Therefore, we briefly introduce the FBG sensing principle. A more detailed explanation can be found in [29].

FBGs are special sections inscribed in optical fibers. Each grating is characterized by a specific Bragg wavelength $\lambda_\mathrm{B}$. It reflects incoming light with exactly this wavelength. However, if the fiber is put under longitudinal stress and/or temperature change, the reflected light spectrum is shifted. The relationship between the wavelength shift $\Delta\lambda_\mathrm{B}$ and $\lambda_\mathrm{B}$ is given by

$$\frac{\Delta\lambda_\mathrm{B}}{\lambda_\mathrm{B}} = (1-p_\mathrm{e})\varepsilon_i + (\alpha_\Lambda + \alpha_\mathrm{n})\Delta T$$

with $\varepsilon_i$ as the strain in the grating $i$, $p_\mathrm{e}$ the strain optic coefficient (typically 0.22), $\alpha_\Lambda$ the thermal expansion coefficient, $\alpha_\mathrm{n}$ the thermo-optic coefficient, and $\Delta T$ the temperature change. In the following, we assume that the sensor array is used in stable temperature conditions and therefore $\Delta T = 0$. Hence, strain is related to wavelength shift by $\varepsilon_i = \frac{\Delta\lambda_\mathrm{B}}{(1-p_\mathrm{e})\lambda_\mathrm{B}}$.

### C. Strain curvature twist model

Let us consider a small section of an undeformed sensor array with circular cross-section at arc length $s$ which has the length $l_0$. This section is referred to as *sensing segment* in the following and is shown in Fig. 1a. It covers the range from $s - \frac{l_0}{2}$ to $s + \frac{l_0}{2}$ and represents a segment of the array, in which strain can be measured. If the array is deformed, we assume, that no deformation of the cross-section occurs. This assumption is valid, if the radius of the sensing segment is much smaller than its length (as it is for FBG multicore fibers).

The strain sensor with index $i$ has constant distance $r$ from the centerline and has the length $l_0$ in the undeformed state. If the sensing segment is elongated, the original longitudinal strain sensor is now stretched by $\Delta l_\mathrm{a}$. Bending the section adds an additional elongation $\Delta l_{\mathrm{b},i}$. Note, that the sensor is still parallel to the centerline of the sensing segment and has now the length $l_\mathrm{long} = l_0 + \Delta l_\mathrm{a} + \Delta l_{\mathrm{b},i}$ as shown in Fig. 2b. Twisting the segment by angle $\Delta\varrho = \varrho\left(s + \frac{l_0}{2}\right) - \varrho\left(s - \frac{l_0}{2}\right)$ deforms the sensor, such that it now has the length $l_{\mathrm{Sens},i} = l_0 + \Delta l_i$. By assuming, that the segment's cross section remains planar and circular after deformation and that it is still perpendicular to the centerline, we can apply the Pythagorean theorem as depicted in Fig. 2b which results in

$$(l_0 + \Delta l_\mathrm{a} + \Delta l_{\mathrm{b},i})^2 + (r\Delta\varrho)^2 = (l_0 + \Delta l_i)^2. \tag{2}$$

Dividing by $l_0^2$ and defining strain as $\varepsilon = \frac{\Delta l}{l_0}$ yields

$$(1 + \varepsilon_\mathrm{a} + \varepsilon_{\mathrm{b},i})^2 + \left(r\frac{\Delta\varrho}{l_0}\right)^2 = (1+\varepsilon_i)^2 \tag{3}$$

with $\Delta l$ the length change after deformation, $\varepsilon_\mathrm{a}$ the strain caused by elongation, $\varepsilon_{\mathrm{b},i}$ the strain in sensor $i$ due to pure bending and $\varepsilon_i$ the actual strain measured by sensor $i$. We get $\varepsilon_\mathrm{a}$ directly from the measurements of the central sensor. By considering only small strains, we can add up $\varepsilon_\mathrm{a}$ and $\varepsilon_{\mathrm{b},i}$.

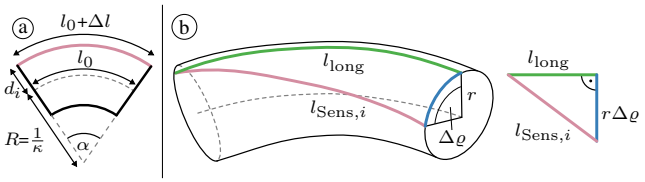


Fig. 2. Deformed sensing segment under: (a) Pure bending with curvature radius $\boldsymbol{R=\kappa^{-1}}$. Length $\boldsymbol{l_0}$ of centerline (dashed) is unaffected by deformation while the sensor $\boldsymbol{i}$ (purple) is stretched by $\boldsymbol{\Delta l}$. $\boldsymbol{d_i}$ is the plumb distance of sensor $\boldsymbol{i}$ to the rectifying plane. (b) Bending, twisting and elongation. Sensor $\boldsymbol{i}$ with distance $\boldsymbol{r}$ from the centerline is shown after elongation and bending (green) as well as after twisting about angle $\boldsymbol{\Delta\varrho}$ (purple). Centerline (dashed) is only affected by elongation.

Let us now focus on the cross-section of the sensor array at arc length $s$ as shown in Fig. 1b. In the case of pure bending (see Fig. 2a), the following equation can be found in literature (e.g. [10]):

$$\varepsilon_{\mathrm{b},i} = -\kappa r\cos(\theta_\mathrm{b} - \theta_i) \tag{4}$$

In the remainder of this paper, we only consider $\theta_\mathrm{b} \in [-\pi, \pi]$. Equation (3) can be rewritten as

$$(E_\mathrm{a} - \kappa r\cos(\theta_\mathrm{b} - \theta_i))^2 + (r\varrho')^2 = E_i^2 \tag{5}$$

with

$$E_\mathrm{a} := 1 + \varepsilon_\mathrm{a}, \qquad E_i := 1 + \varepsilon_i, \qquad \varrho' = \frac{\mathrm{d}\varrho}{\mathrm{d}s} \approx \frac{\Delta\varrho}{l_0}$$

Rearranging leads to

$$E_\mathrm{a} - \kappa r\cos(\theta_\mathrm{b} - \theta_i) = \delta_i\sqrt{E_i^2 - (r\varrho')^2} \tag{6}$$

with $\delta_i := \pm 1$ representing an ambiguity caused by taking the square root. Considering only real values during calculation, the sign of the right side of (6) is completely determined by $\delta_i$. Let us assume $\delta_i = -1$. Then, the following inequality must be fulfilled:

$$E_\mathrm{a} - \kappa r\cos(\theta_\mathrm{b} - \theta_i) \leq 0 \tag{7}$$

Using the definitions depicted in Fig. 2a yields

$$\frac{l_0}{R} = \alpha = \frac{l_0 + \Delta l}{R + d_i} \qquad \Rightarrow \qquad \frac{\Delta l}{l_0} = \frac{d_i}{R} = \kappa d_i \tag{8}$$

Under pure bending, $d_i$ is the plumb distance from sensor $i$ to the rectifying plane and varies between 0 and $r$. The maximum strain occurs, if $d_i = r$ (see Fig. 1b). By defining $\varepsilon_\mathrm{max} = \frac{\Delta l_\mathrm{max}}{l_0} = \kappa r$, (7) can be rewritten as

$$1 \leq \varepsilon_\mathrm{max}\cos(\theta_\mathrm{b} - \theta_i) - \varepsilon_\mathrm{a}. \tag{9}$$

For conventional silica glass as used in optical fibers, $|\varepsilon_\mathrm{max}|$ should not exceed 1 %, hence (9) can never be fulfilled. Moreover, even if unrealistic large values for $\varepsilon_\mathrm{max}$ and $\varepsilon_\mathrm{a}$ are considered (e.g. 40 %), no solution is found. In contrast, performing the same analysis for $\delta_i = +1$ yields

$$1 \geq \varepsilon_\mathrm{max}\cos(\theta_\mathrm{b} - \theta_i) - \varepsilon_\mathrm{a} \tag{10}$$

which is true for typical strain values in silica glass. Therefore, only $\delta_i = +1$ is further considered.

Rearranging (6) yields

$$\kappa = \frac{-1}{r\cos(\theta_\mathrm{b}-\theta_i)}\left(\sqrt{E_i^2-(r\varrho')^2}-E_\mathrm{a}\right). \tag{11}$$

It is obvious, that (11) is only valid, if $\theta_\mathrm{b}-\theta_i \neq (2n+1)\frac{\pi}{2}$ with $n \in \mathbb{Z}$. Therefore, if one of the sensor cores lies in the rectifying plane, it can not be used to calculate $\kappa$. To improve readability we define

$$A_i \coloneqq \sqrt{E_i^2-(r\varrho')^2}-E_\mathrm{a}, \quad \mathrm{s}_x \coloneqq \sin(\theta_x), \quad \mathrm{c}_x \coloneqq \cos(\theta_x)$$

Using two of the three available strain measurements denoted with the indices $u$ and $v$ with $u \neq v$, we can remove $\kappa$ from (11) by setting the two terms equal:

$$\cos(\theta_\mathrm{b}-\theta_v)A_u = \cos(\theta_\mathrm{b}-\theta_u)A_v \tag{12}$$

Using trigonometric identity $\cos(\theta_\mathrm{b}-\theta_i) = \mathrm{c}_\mathrm{b}\,\mathrm{c}_i + \mathrm{s}_\mathrm{b}\,\mathrm{s}_i$ we get

$$\frac{\sin(\theta_\mathrm{b})}{\cos(\theta_\mathrm{b})} = \tan(\theta_\mathrm{b}) = \frac{A_v\,\mathrm{c}_u - A_u\,\mathrm{c}_v}{A_u\,\mathrm{s}_v - A_v\,\mathrm{s}_u} \tag{13}$$

which allows to calculate $\theta_\mathrm{b}$ with the inverse tangent function.

To calculate $\varrho'$, we use all three strain measurements. Thus, one can select two different tuples for $(u, v)$ to insert into (13). Without loss of generality, we choose the indices $(1, 2)$ and $(1, 3)$. Setting both equations equal results in

$$\frac{A_2\,\mathrm{c}_1 - A_1\,\mathrm{c}_2}{A_1\,\mathrm{s}_2 - A_2\,\mathrm{s}_1} = \frac{A_3\,\mathrm{c}_1 - A_1\,\mathrm{c}_3}{A_1\,\mathrm{s}_3 - A_3\,\mathrm{s}_1} \tag{14}$$

Rearranging (14) and defining

$$\mathrm{s}_{xy} \coloneqq \sin(\theta_x-\theta_y) = \mathrm{s}_x\,\mathrm{c}_y - \mathrm{s}_y\,\mathrm{c}_x$$

yields

$$0 = A_1 \cdot (A_1\,\mathrm{s}_{23} + A_2\,\mathrm{s}_{31} + A_3\,\mathrm{s}_{12}). \tag{15}$$

To calculate the solutions for $\varrho'$, each factor of (15) is set equal to zero. Beginning with the first factor, the following equation must be solved:

$$A_1 = \sqrt{E_1^2-(r\varrho')^2}-E_\mathrm{a} = 0 \tag{16}$$

which results in

$$|\varrho'| = \frac{1}{r}\sqrt{E_1^2-E_\mathrm{a}^2}. \tag{17}$$

Because $i = 1$ was arbitrarily chosen, (17) must be valid for all $E_i$. This is only true, if the strains in all sensors are equal, hence the sensing segment is only affected by torsion and no bending occurs.

Setting the second factor of (15) equal to zero, gives

$$A_1\,\mathrm{s}_{23} + A_2\,\mathrm{s}_{31} + A_3\,\mathrm{s}_{12} = 0. \tag{18}$$

Assuming only small strain values, (18) can be linearized by performing a Taylor series expansion around $\varepsilon_i = 0$ and stopping after the first order term. By using

$$\begin{aligned} A_i\big|_{\varepsilon_i=0} &= \sqrt{1-(r\varrho')^2}-E_\mathrm{a} \\ \left.\frac{\partial A_i}{\partial \varepsilon_i}\right|_{\varepsilon_i=0} &= \frac{1}{\sqrt{1-(r\varrho')^2}} \\ \frac{\partial A_u}{\partial \varepsilon_v} &= 0 \text{ for } u \neq v \end{aligned}$$

we can write (18) as

$$\begin{aligned} \mathrm{s}_{23}\,\varepsilon_1 \left.\frac{\partial A_1}{\partial \varepsilon_1}\right|_{\varepsilon_1=0} + \mathrm{s}_{31}\,\varepsilon_2 \left.\frac{\partial A_2}{\partial \varepsilon_2}\right|_{\varepsilon_2=0} + \mathrm{s}_{12}\,\varepsilon_3 \left.\frac{\partial A_3}{\partial \varepsilon_3}\right|_{\varepsilon_3=0} \\ + \mathrm{s}_{23}\,A_1\big|_{\varepsilon_1=0} + \mathrm{s}_{31}\,A_2\big|_{\varepsilon_2=0} + \mathrm{s}_{12}\,A_3\big|_{\varepsilon_3=0} \approx 0 \end{aligned} \tag{19}$$

Substituting and rearranging (19) leads to

$$0 = (\sqrt{1-(r\varrho')^2})^2 - E_\mathrm{a}\sqrt{1-(r\varrho')^2} + Q \tag{20}$$

with

$$Q \coloneqq \frac{\varepsilon_1\,\mathrm{s}_{23} + \varepsilon_2\,\mathrm{s}_{31} + \varepsilon_3\,\mathrm{s}_{12}}{\mathrm{s}_{23} + \mathrm{s}_{31} + \mathrm{s}_{12}} \tag{21}$$

Solving for $\sqrt{1-(r\varrho')^2}$ results in

$$\sqrt{1-(r\varrho')^2} = \frac{E_\mathrm{a}}{2} + \delta_\mathrm{G}\sqrt{\left(\frac{E_\mathrm{a}}{2}\right)^2 - Q} \tag{22}$$

with $\delta_\mathrm{G} = \pm 1$. Squaring both sides and rearranging finally leads to

$$|\varrho'| = \frac{1}{r}\sqrt{1-\left(\frac{E_\mathrm{a}}{2} + \delta_\mathrm{G}\sqrt{\left(\frac{E_\mathrm{a}}{2}\right)^2 - Q}\right)^2} \tag{23}$$

Inspecting (17) and (23), we realize that there is always a positive and negative solution for $\varrho'$. This is caused by the coaxial alignment of the sensing cores with respect to the centerline. Imagine an unbent and untwisted rod equipped with a coaxial strain sensor. Twisting the rod clockwise or counterclockwise will result in the same sensor measurement. Therefore, the twisting direction can not be determined with this sensor arrangement and must be known in advance.

Using (11), (13), (17) and (23) one can then calculate the curve parameters for the current sensing segment at arc length $s$. Parameter $\delta_\mathrm{G}$ is selected so that (13) yields the same results for all possible combinations of the indices $u$ and $v$. The strain sensors give a distinct measurement $\varepsilon_i(s_\mathrm{k})$ at the sensing segment position $s_\mathrm{k}$. Interpolating $\varepsilon_i(s_\mathrm{k})$ between all cross-sections, allows to calculate the curve parameters for all $s$ between the first and the last sensing segment. By solving (1), the centerline of the sensing segment is finally calculated.

After the calculations, it may occur, that $\kappa < 0$. However, per definition $\kappa$ must be greater or equal 0. If $\kappa$ is negative, it must be multiplied with $-1$ and $\pi$ must be added to $\theta_\mathrm{b}$. The legitimacy of this transformation can be shown with the help of the curvature vector $\boldsymbol{\kappa}$ (see Fig. 1b):

$$\boldsymbol{\kappa} = \kappa\begin{bmatrix}\cos(\theta_\mathrm{b})\boldsymbol{n}_1 \\ \sin(\theta_\mathrm{b})\boldsymbol{n}_2\end{bmatrix} = -\kappa\begin{bmatrix}\cos(\theta_\mathrm{b}+\pi)\boldsymbol{n}_1 \\ \sin(\theta_\mathrm{b}+\pi)\boldsymbol{n}_2\end{bmatrix} \tag{24}$$

Hence, the transformation does not change $\boldsymbol{\kappa}$.

To investigate the error in $\varrho'$ induced by linearization, we calculate $\varrho'$ before linearization numerically from (18) using Matlab's `fsolve` function and after linearization in closed-form from (23). This yields $\varrho'_\mathrm{num}$ and $\varrho'_\mathrm{cf}$, receptively. In these calculations, we assume $\theta_2-\theta_3 = \theta_3-\theta_1 = \theta_1-\theta_2 = 120\,^\circ$, $r = 38\,\mu\mathrm{m}$, $\varepsilon_\mathrm{a} = 0$ and that the strain in all outer sensors is equal. The relative twist deviation $\Delta\varrho'_\mathrm{rel} = |\varrho'_\mathrm{num} - \varrho'_\mathrm{cf}| \cdot \varrho'^{-1}_\mathrm{num}$ is shown in Fig. 3. For typical strain values in silica glass, $\Delta\varrho'_\mathrm{rel}$ is below $0.01\,\%$ and for strain values $\leq 10^{-5}$ it is zero. Hence, the induced error can be neglected.

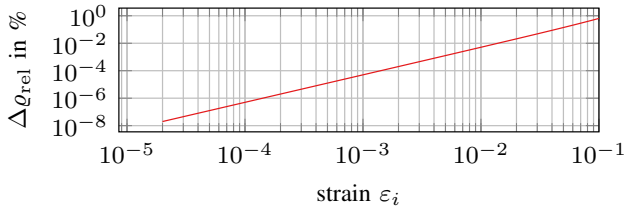


Fig. 3. Relative twist deviation $\boldsymbol{\Delta\varrho'_{\mathrm{rel}}}$ for given strain values $\boldsymbol{\varepsilon_i}$ and $\boldsymbol{r = 38\,\mu\mathrm{m}}$. For $\boldsymbol{\varepsilon_i \leq 10^{-5}}$, $\boldsymbol{\Delta\varrho'_{\mathrm{rel}}}$ is zero.

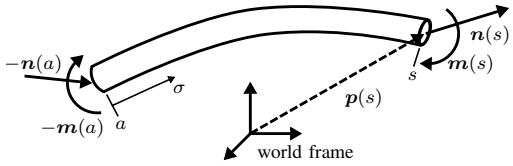


Fig. 4. Deformed rod. The coordinate of the rod's centerline at arc length $\boldsymbol{s}$ is described in world frame by vector $\boldsymbol{p(s)}$. At this point, external forces $\boldsymbol{n(s)}$ and torques $\boldsymbol{m(s)}$ act on the rod.

## III. Evaluation of Shape Reconstruction

To evaluate our algorithm, we perform several simulations by calculating simulated sensor strain values based on a synthetic fiber centerline. In general, the centerline can be chosen arbitrarily, as long as it is three times differentiable.

We simulate the synthetic centerline by implementing a Cosserat rod model. The benefit of this approach is, that twisting is modeled physically. Hence, the deformation of a fiber, which is placed in parallel to the centerline in the cross-section will also deform in a realistic manner. This parallel fiber is used to calculate simulated strain values.

We then compare our strain curvature model to two other approaches commonly found in the literature. All algorithms are implemented in Matlab 2019b. Systems of ordinary differential equations are solved with Runge-Kutta (4,5) as implemented in Matlab's `ode45` function. To apply the shooting method presented in section III-A, we rely on the trust-region dogleg optimization algorithm as implemented in Matlab's `fsolve` function.

### A. Cosserat rod model

In this section we give a brief overview of the kinematics of a simple Cosserat rod with a circular cross-section as depicted in Fig. 4. A more detailed discussion can be found in [30]. The rod shape is described with respect to the arc length $s \in [0, L]$ by its centerline $\boldsymbol{p}(s) \in \mathbb{R}^3$ and a corresponding material frame with the orientation $\boldsymbol{R}(s) = [\boldsymbol{e}_1, \boldsymbol{e}_2, \boldsymbol{e}_3] \in \mathrm{SO}(3)$. The vector $\boldsymbol{e}_3$ is coaxial to the rod centerline's tangent vector. Furthermore, $\boldsymbol{u}(s)$ and $\boldsymbol{v}(s)$ are the angular and translational rate of change of this frame with respect to $s$. The initial straight rod is deformed by distinct forces $\boldsymbol{n}(s)$ and torques $\boldsymbol{m}(s)$ which act on the rod at $s$ (distributed loads are neglected). Assuming, that no warping occurs (i.e. the cross-section remains plane) and according to [17], the explicit model equations are given by

$$\begin{aligned}
\boldsymbol{p}'(s) &= \boldsymbol{R}(s)\boldsymbol{v}(s), & \boldsymbol{v}(s) &= \boldsymbol{K}_{\mathrm{se}}(s)^{-1}\boldsymbol{R}(s)^{\mathrm{T}}\boldsymbol{n}(s)\\
\boldsymbol{R}'(s) &= \boldsymbol{R}(s)\widehat{\boldsymbol{u}}(s), & \boldsymbol{u}(s) &= \boldsymbol{K}_{\mathrm{bt}}(s)^{-1}\boldsymbol{R}(s)^{\mathrm{T}}\boldsymbol{m}(s)\\
\boldsymbol{n}'(s) &= 0, & \boldsymbol{m}'(s) &= -\boldsymbol{p}'(s)\times\boldsymbol{n}(s)
\end{aligned} \tag{25}$$

with $\boldsymbol{u}(s) = [u_1, u_2, u_3]^{\mathrm{T}}$ and

$$\widehat{\boldsymbol{u}}(s) = \begin{bmatrix} 0 & -u_3 & u_2 \\ u_3 & 0 & -u_1 \\ -u_2 & u_1 & 0 \end{bmatrix}$$

$$\boldsymbol{K}_{\mathrm{se}}(s) = \mathrm{diag}(GA(s), GA(s), EA(s))$$

$$\boldsymbol{K}_{\mathrm{bt}}(s) = \mathrm{diag}\left(EI_{xx}(s), EI_{yy}(s), G\left(I_{xx}(s) + I_{yy}(s)\right)\right)$$

Here, $\boldsymbol{K}_{\mathrm{se}}(s)$ and $\boldsymbol{K}_{\mathrm{bt}}(s)$ are the stiffness matrices of shear and extension as well as bending and torsion, respectively. They are a function of the Young's modulus $E$, the shear modulus $G$, the rod's cross-section $A(s)$ and the second moments of area $I_{xx}(s)$ and $I_{yy}(s)$.

Although, the rod's model equations (25) are defined in the world frame, it can be convenient to express forces and torques acting on the rod in the orientation of the material frame. For example, one can assure, that a force acts only perpendicular to the centerline or that a torque acts only around the centerline's tangent vector. Hence, $\tilde{\boldsymbol{n}}(s)$ and $\tilde{\boldsymbol{m}}(s)$ are forces and torques at the point $\boldsymbol{p}(s)$ expressed as a linear combination of $\boldsymbol{e}_1$,$\boldsymbol{e}_2$ and $\boldsymbol{e}_3$. They can be converted to forces and torques oriented in world frame by $\boldsymbol{n}(s) = \boldsymbol{R}(s)\tilde{\boldsymbol{n}}(s)$ and $\boldsymbol{m}(s) = \boldsymbol{R}(s)\tilde{\boldsymbol{m}}(s)$.

In the remainder of this paper, only point forces $\boldsymbol{F}(s)$ and torques $\boldsymbol{M}(s)$ are applied on the rod at distinct locations $s = \tilde{s}$. This results in a discontinuity of $\boldsymbol{n}(s)$ and $\boldsymbol{m}(s)$ at $\tilde{s}$:

$$\begin{aligned}
\boldsymbol{n}(\tilde{s}^-) &= \boldsymbol{F}(\tilde{s}) + \boldsymbol{n}(\tilde{s}^+)\\
\boldsymbol{m}(\tilde{s}^-) &= \boldsymbol{M}(\tilde{s}) + \boldsymbol{m}(\tilde{s}^+)
\end{aligned}$$

with $\tilde{s}^-$ and $\tilde{s}^+$ being locations right before and after $\tilde{s}$.

The rod equations (25) are solved with a shooting method. We define arbitrary start values for $\boldsymbol{p}(0)$ and $\boldsymbol{R}(0)$ and vary the start values for $\boldsymbol{n}(0)$ and $\boldsymbol{m}(0)$ until the residuum between the calculated force $\boldsymbol{n}_{\mathrm{calc}}(s_{\mathrm{end}})$ and torque $\boldsymbol{m}_{\mathrm{calc}}(s_{\mathrm{end}})$ at the rod tip and the given values $\boldsymbol{F}(s_{\mathrm{end}})$ and $\boldsymbol{M}(s_{\mathrm{end}})$ fall below a pre-defined threshold.

The position $\boldsymbol{p}_i(s)$ of each a outer sensor $i$ in the rod's cross-section at $s$ is then calculated by

$$\boldsymbol{p}_i(s) = \boldsymbol{p}(s) + r\cos(\theta_i)\boldsymbol{e}_1(s) + r\sin(\theta_i)\boldsymbol{e}_2(s) \tag{26}$$

which allows to estimate the sensor strain at position $s$ by

$$\varepsilon_i(s) = \int_{s-\frac{1}{2}l_0}^{s+\frac{1}{2}l_0} \frac{\|\boldsymbol{p}_i'(\sigma)\|}{l_0}\,\mathrm{d}\sigma - 1 \tag{27}$$

with $l_0$ being the length of the strain sensor in undeformed state and $\|\boldsymbol{a}\|$ the Euclidean norm of vector $\boldsymbol{a}$. The strain $\varepsilon_{\mathrm{a}}(s)$ in the central sensor can be calculated analogously by replacing $\boldsymbol{p}_i'(\sigma)$ with $\boldsymbol{p}'(\sigma)$ in (27).

To compare the reconstructed centerline with the ground truth centerline of the rod model, we use the relative shape deviation $e_{\mathrm{rel}}$

$$e_{\mathrm{rel}} = \frac{\|\boldsymbol{\gamma}(s) - \boldsymbol{p}(s)\|}{s - s_0} \tag{28}$$

where $s_0$ is the arc length of the rod model at which the first sensing segment is located. Furthermore, we define the relative arc length $s_{\mathrm{rel}}$ as

$$s_{\mathrm{rel}} = \frac{s - s_0}{s_{\mathrm{end}} - s_0} \tag{29}$$

### B. Reference strain curvature models

To validate our algorithm (denoted as *Twist* model), we compare it with two approaches from the literature. We only interchange the different strain curvature models, hence to reconstruct the centerline, we always rely on the algorithm described in section II-A.

The first model is presented by Moore and Rogge [10], which we denote as *Moore*. It solves the equation system defined by (4). Because twist is not considered in this model, strain measured in the sensing segment is interpreted as bending strain and henceforth $\varepsilon_{\mathrm{b}_i} = \varepsilon_i$. The main idea is to create an apparent curvature vector $\boldsymbol{\kappa}_{\mathrm{app}}$ which lies in the cross-section of the sensing segment spanned by $\boldsymbol{n}_1$ and $\boldsymbol{n}_2$. To avoid dealing with trigonometric equations while deriving the model and in contrast to [10], we transform this vector in the complex plane with $\boldsymbol{n}_1$ and $\boldsymbol{n}_2$ being the real and complex axis, respectively and with $j$ as the imaginary unit:

$$\boldsymbol{\kappa}_{\mathrm{app}} = -\sum_{i=1}^{3} \frac{\varepsilon_i}{r}\,\mathrm{c}_i\,\boldsymbol{n}_1 - \sum_{i=1}^{3} \frac{\varepsilon_i}{r}\,\mathrm{s}_i\,\boldsymbol{n}_2 = -\sum_{i=1}^{3} \frac{\varepsilon_i}{r} e^{j\theta_i}. \tag{30}$$

To improve readability, we further omit the sub- and superscript of the summation symbol. In the remainder of this section, it always sums up from 1 to 3 over $i$ . Starting from the equation system defined by (4) we can rewrite the equations as complex functions

$$\varepsilon_i = -\frac{\kappa}{2} r \left( e^{j(\theta_{\mathrm{b}} - \theta_i)} + e^{-j(\theta_{\mathrm{b}} - \theta_i)} \right). \tag{31}$$

Rearranging results in

$$-r^{-1}\varepsilon_i e^{j\theta_i} = \frac{\kappa}{2}\left( e^{j\theta_{\mathrm{b}}} + e^{-j\theta_{\mathrm{b}}} e^{j2\theta_i} \right). \tag{32}$$

Summing up over $i$ yields an expression for $\boldsymbol{\kappa}_{\mathrm{app}}$:

$$\boldsymbol{\kappa}_{\mathrm{app}} = -\sum \frac{\varepsilon_i}{r} e^{j\theta_i} = \frac{\kappa}{2}\left( 3e^{j\theta_{\mathrm{b}}} + e^{-j\theta_{\mathrm{b}}} \sum e^{j2\theta_i} \right). \tag{33}$$

The relation $\theta_i = \theta_1 + \frac{2\pi}{3}(i-1)$ holds, if the outer sensors are equally spaced in the cross-section. In this case, (33) can be written as

$$\boldsymbol{\kappa}_{\mathrm{app}} = \frac{\kappa}{2}\left( 3e^{j\theta_{\mathrm{b}}} + e^{-j\theta_{\mathrm{b}}} e^{j(2\theta_1 - \frac{4\pi}{3})} \sum (e^{j\frac{4}{3}\pi})^i \right). \tag{34}$$

The remaining sum in (34) is a finite geometric series and can be simplified to

$$\sum (e^{j\frac{4}{3}\pi})^i = e^{j\frac{4}{3}\pi}\left( e^{j\frac{4}{3}\pi} - 1 \right)^{-1} \left( e^{j4\pi} - 1 \right) = 0. \tag{35}$$

Hence, we arrive at

$$\boldsymbol{\kappa}_{\mathrm{app}} = -\sum \frac{\varepsilon_{\mathrm{b}_i}}{r} e^{j\theta_i} = \frac{3}{2}\kappa e^{j\theta_{\mathrm{b}}} \tag{36}$$

and therefore

$$\kappa = \frac{2}{3}|\boldsymbol{\kappa}_{\mathrm{app}}| \qquad \theta_{\mathrm{b}} = \arg(\boldsymbol{\kappa}_{\mathrm{app}}) \tag{37}$$

This approach has the advantage, that all strain measurements are used to calculate $\kappa$ and $\theta_{\mathrm{b}}$ which reduces the influence of measurement noise simultaneously present in all sensors.

Another model found commonly in literature extends (4) by adding $\varepsilon_{\mathrm{add}}$, which compensates for additional strains caused by temperature changes or external loads. This leads to the following equation system

$$-\varepsilon_{\mathrm{b}_i} - \kappa r \cos(\theta_{\mathrm{b}} - \theta_i) = \varepsilon_{\mathrm{add}}. \tag{38}$$

We denote this furthermore as the *Classic* model. Again, twist is not considered and therefore $\varepsilon_{\mathrm{b}_i} = \varepsilon_i$. Plugging in two arbitrary indices $i = u$ and $i = v$ into (38) and setting those equations equal yields

$$\kappa = \frac{\varepsilon_v - \varepsilon_u}{2r \sin\left(0.5\left(\theta_u - \theta_v\right)\right) \sin\left(\theta_{\mathrm{b}} - 0.5\left(\theta_u + \theta_v\right)\right)}. \tag{39}$$

Equation (39) must yield the same result for every combination of indices. By using two arbitrary sets for $(u, v)$ (e.g. $(1, 2)$ and $(1, 3)$) and setting the resulting terms equal, we get

$$\tan\theta_{\mathrm{b}} = -\frac{\varepsilon_1(\mathrm{c}_2 - \mathrm{c}_3) + \varepsilon_2(\mathrm{c}_3 - \mathrm{c}_1) + \varepsilon_3(\mathrm{c}_1 - \mathrm{c}_2)}{\varepsilon_1(\mathrm{s}_2 - \mathrm{s}_3) + \varepsilon_2(\mathrm{s}_3 - \mathrm{s}_1) + \varepsilon_3(\mathrm{s}_1 - \mathrm{s}_2)}. \tag{40}$$

Using the inverse tangent function yields the value for $\theta_{\mathrm{b}}$. Note, that $\kappa$ is only defined if $\frac{1}{2}\left(\theta_u - \theta_v\right) \neq n\pi$ and $\theta_{\mathrm{b}} - \frac{1}{2}\left(\theta_u + \theta_v\right) \neq n\pi$ with $n \in \mathbb{Z}$. Hence, the indices $u$ and $v$ must be selected appropriately.

As presented above, the models Moore and Classic are derived from nearly the same initial system of equations. Both models do not take material twist into account. While Moore assumes strictly pure bending, Classic allows to compensate noise in strain measurements, which occurs equally in all sensors. In comparison, our model Twist explicitly accounts for twist and elongation and considers their non-linear contribution to the sensor measurements.

### C. Simulation parameters

To evaluate our method, we simulate a slender rod with constant circular cross-section (radius: 1 mm, length: 320 mm, Young's modulus: 70 GPa, Shear modulus: 30 GPa). The rod model is solely used to calculate a realistic centerline. It is not intended to model the sensor array (e.g. as optical fiber). Hence, the rod's material properties are arbitrarily chosen.

We distribute 32 sensing segments along the rod's centerline, each containing three outer strain sensors equally distributed in the sensor array's cross-section at a radial distance of $r = 38\,\mu\mathrm{m}$ from the centerline with $\theta_i = [30°, 150°, 270°]$ and a central sensor. All sensors have a length of $l_0 = 5\,\mathrm{mm}$. Furthermore, all sensing segments of the sensor array are equally spaced along the centerline with a spacing of 10 mm. Hence, the middle points of the first and last sensing segment are located at $s_0 = 5\,\mathrm{mm}$ and $s_{\mathrm{end}} = 315\,\mathrm{mm}$, respectively. The chosen values are based on material dimensions of commercially available FBG multicore fibers.

### D. Case I: Pure bending

To create different shaped centerlines, simulated forces act on the rod at different $\boldsymbol{p}(s)$. We denote a combination of such

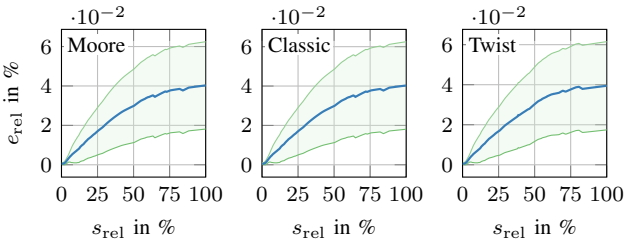


Fig. 5. Simulation result for 115 force sets in case of pure bending. Depicted are the mean (blue line), as well as the area between ± one standard deviation (green area) of the relative shape deviation.

forces as a force set. Each set consists of at least one and at most three forces $\tilde{\boldsymbol{n}}(s)$, where $m$ is the number of forces. One force is always placed at the rod tip. To assure, that these forces always act perpendicular on the centerline, they are expressed in the rod's material frame:

$$\tilde{\boldsymbol{n}}(s) = F\left(\cos(\alpha)\boldsymbol{e}_1(s) + \sin(\alpha)\boldsymbol{e}_2(s)\right) \tag{41}$$

with $F$ being the force magnitude and $\alpha$ the force direction in the $\boldsymbol{e}_1$-$\boldsymbol{e}_2$ plane. To vary the resulting shapes, each force set is created with the help of uniform random distributions. For each set, four parameters are varied: the number of forces $m$, their magnitude $F$, their direction $\alpha$ in the cross-section and the arc length $s$, at which they act on the rod. The force magnitude $F$ varies between 0.1 and 3 N and $\alpha$ is drawn from the interval $[0, 2\pi]$. To assure, that two forces do not act on the same rod position, the arc length is divided in $m$ segments and in each segment, only a single force is allowed. For 115 simulated force sets, the mean of the relative shape deviation as well as its standard deviation are calculated and depicted in Fig. 5. All three models show a comparable, small shape deviation. The maximum mean error of the models Classic and Moore is 0.040 %, while for our model Twist it is 0.039 %. The numerical calculation of the simulated strain values induces small deviations from the ideal strain values. These inaccuracies accumulate along the rod length which results in an increasing shape deviation. However, under pure bending, all algorithms perform equal. In this special case the three models solve the same system of equations, just in a different manner. Under pure bending, no twist or elongation acts on the sensor array ($\varrho' = 0$, $\varepsilon_{\mathrm{a}} = 0$) and no additional strain except of bending strain occurs ($\varepsilon_{\mathrm{add}} = 0$, $\varepsilon_{\mathrm{b}_i} = \varepsilon_i$). Plugging in these constraints into the initial equations of models Twist (5) and Classic (38) yields exactly the same initial formulas as for model Moore (4).

### E. Case II: Bending and twisting

To validate the influence of twisting on the reconstruction algorithm, we extend the simulations of section III-D by applying different torques at the rod tip. Hence, each of the 115 force sets is extended by a torque $\tilde{\boldsymbol{m}}(s_{\mathrm{end}}) = [0, 0, M]^{\mathrm{T}}$, which is located at the rod end $\boldsymbol{p}(s_{\mathrm{end}})$ and which acts around the rods tangent vector. This variation is performed several times with different torque magnitudes $M = [0.01, 0.03, 0.05, 0.1, 0.15, 0.2]\mathrm{Nm}$. These torques cause a twisting between the material frame at the rod tip and base of approximately 4°, 12°, 19°, 39°, 58° and 78°, respectively. The mean of the relative shape deviation of the various simulations is shown in Fig. 6.

It is apparent, that the maximum mean shape deviation of models Moore and Classic grew with increasing applied tip torque. For a tip torque of 0.01 Nm (corresponds to a twist rate of about $\varrho' = 12.5\,^{\circ}/\mathrm{m}$) the maximum mean shape deviation is about 1.7 % and already increases to 5.0 % for a tip torque of 0.03 Nm ($\varrho' = 37.5\,^{\circ}/\mathrm{m}$). In comparison, the mean shape deviation of model Twist does never exceed 0.04 %, even for a large tip torque of 0.20 Nm ($\varrho' = 243.75\,^{\circ}/\mathrm{m}$). Hence, our approach gives more precise results, which are consistent for various simulation runs.

### F. Case III: Bending, twisting and elongation

Furthermore, we evaluate the influence of elongation on the shape reconstruction. To elongate the simulated rods, we extend each of the 115 force sets by an additional force $\tilde{\boldsymbol{n}}(s_{\mathrm{end}}) = [0, 0, 5]^{\mathrm{T}}\mathrm{N}$ at the rod tip which acts along the tangent vector of the centerline. To twist the sensor array, we apply a tip torque of $\tilde{\boldsymbol{m}}(s_{\mathrm{end}}) = [0, 0, 0.20]^{\mathrm{T}}\mathrm{Nm}$. This results in strain in the central sensor of up to $2.28{\cdot}10^{-5}$. The outcome of these simulations are shown in Fig. 7. In comparison to the simulations with the same force sets and a tip torque of 0.20 Nm from section III-E (see Fig. 6f), the mean of the relative shape deviation increases for all models. While the value at the tip for models Moore and Classic increases from 32.7 % to 36.4 %, the mean of the relative tip error for Twist increases from 0.03 % to 0.06 %. Hence, the influence of elongation reduces the accuracy of for all shape sensing algorithms. But for the model Twist the overall accuracy is several orders of magnitude better than for the other two models.

## IV. Sensitivity of Curvature Models

In this section, the sensitivity of the strain curvature models with respect to various disturbances is investigated. In particular, we perform a locale sensitivity analysis of a single sensing segment.

Deviations of the curve parameters ($\kappa$, $\theta_{\mathrm{b}}$ and $\varrho'$) can be caused by errors in strain measurements $\varepsilon_i$ and by an imperfect calibrated distance $r$ between the centerline of the sensor array and the specific sensor [31]. Sensitivity of a quantity is defined as its partial derivative with respect to the source of deviation. Together with the systematic errors of the measurement system, it is used during calculation of error propagation [32].

We calculate six sensitivity values, namely the partial derivatives of the curve parameters with respect to $r$ and $\varepsilon_1$:

$$\partial_\varepsilon \theta_{\mathrm{b}} := \frac{\partial \theta_{\mathrm{b}}}{\partial \varepsilon_1}, \qquad \partial_\varepsilon \kappa := \frac{\partial \kappa}{\partial \varepsilon_1}, \qquad \partial_\varepsilon |\varrho'| := \frac{\partial |\varrho'|}{\partial \varepsilon_1}$$
$$\partial_r \theta_{\mathrm{b}} := \frac{\partial \theta_{\mathrm{b}}}{\partial r}, \qquad \partial_r \kappa := \frac{\partial \kappa}{\partial r}, \qquad \partial_r |\varrho'| := \frac{\partial |\varrho'|}{\partial r}$$

The equations for all investigated models are given in appendix I. For the sake of brevity, we only provide the sensitivities with respect to the strain $\varepsilon_1$. The effect of the other strain measurements can be found analogously.

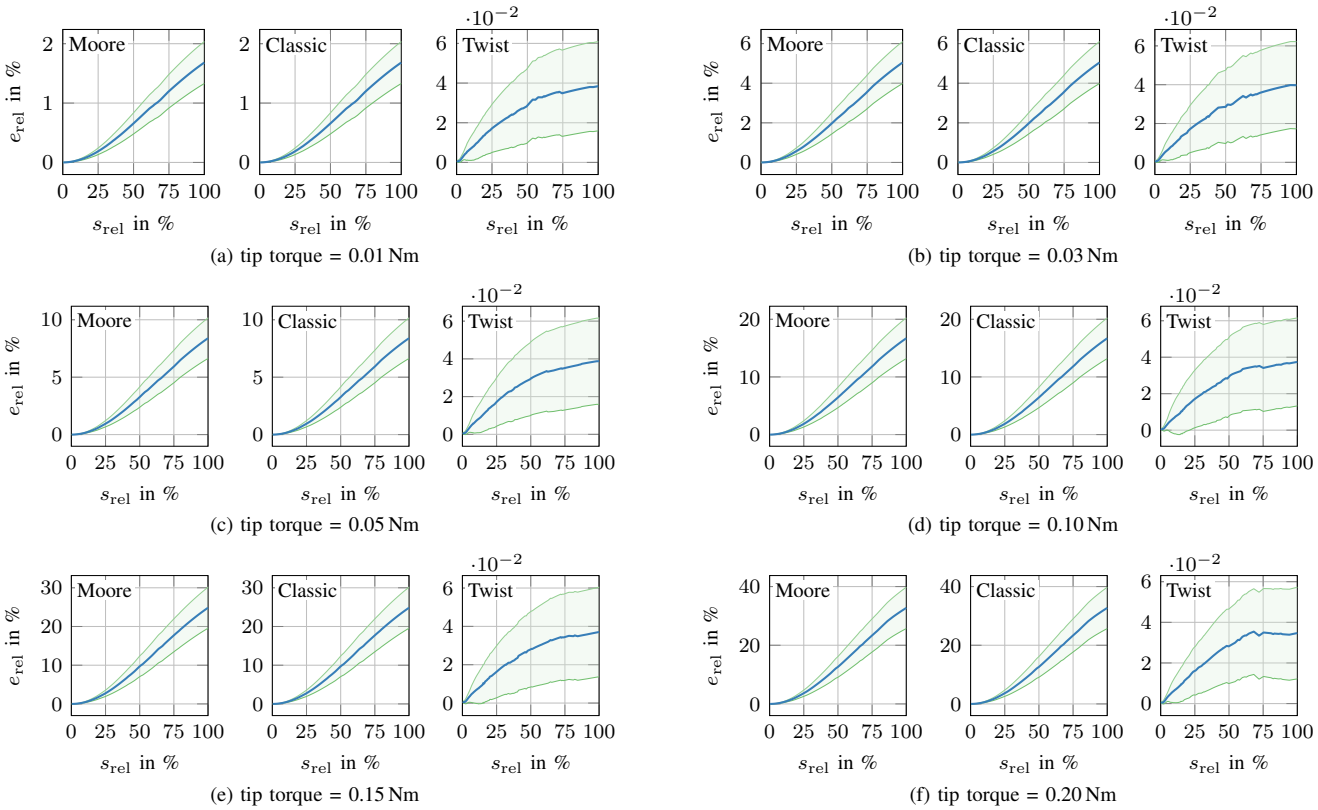


(a) tip torque = 0.01 Nm (b) tip torque = 0.03 Nm (c) tip torque = 0.05 Nm (d) tip torque = 0.10 Nm (e) tip torque = 0.15 Nm (f) tip torque = 0.20 Nm

Fig. 6. Relative shape deviation in case of different tip torques. Depicted are the mean (blue line) and the area between ± one standard deviation (green area) of the relative shape deviation for 115 simulations each. Note, that the scaling of the ordinate differs between model Twist and the other two models.

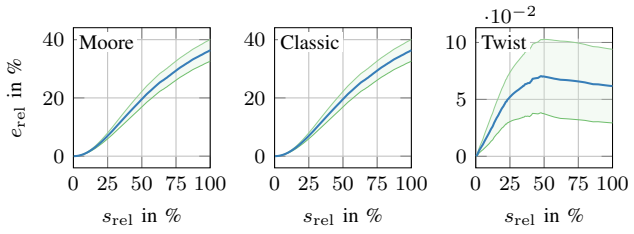


Fig. 7. Simulation result for 115 force sets in case of bending, twisting and elongation. Depicted are the mean (blue line), as well as the area between ± one standard deviation (green area) of the relative shape deviation.

The calculated sensitivities are only valid at a specific operational point, which is defined by a given set of strain values $\varepsilon_i$. These values are calculated after rearranging (5):

$$\varepsilon_i = \sqrt{\left(E_{\mathrm{a}} - \kappa r \cos(\theta_{\mathrm{b}} - \theta_i)\right)^2 + (r\varrho')^2} - 1 \qquad (42)$$

In the remainder of this section we set $E_{\mathrm{a}} = 1$, $r = 38\,\mu\mathrm{m}$ and $\theta_i = [0°, 120°, 240°]$. However, $\theta_{\mathrm{b}}$, $\kappa$ and $\varrho'$ are varied to simulate different operational points. The sensitivity values $\partial_\varepsilon|\varrho'|$ and $\partial_r|\varrho'|$ are not defined for the models Moore and Classic.

In a first set of simulations we calculate the sensitivity values at various operational points in the range of $\kappa \in [2\,\mathrm{m}^{-1}, 20\,\mathrm{m}^{-1}]$ and $\theta_{\mathrm{b}} \in [0°, 180°]$ with $\varrho' = 0.1\,°/\mathrm{m}$. Because untwisted or only slightly twisted sensor arrays represent a common use case in shape reconstruction applications, we want to show the behavior of our model in the bent but (nearly) untwisted state. However, sensitivity $\partial_\varepsilon|\varrho'|$ is not well defined at $\varrho' = 0$, hence we use an operational point close to zero instead, which results in a very slightly twisted sensor array. In Fig. 8 the sensitivities of the different models are shown.

The values for models Moore and Classic are the same, hence Fig. 8a is representative for both models. In Fig. 8b one can see, that the model Twist yields the same values for $\partial_\varepsilon\theta_{\mathrm{b}}$, $\partial_\varepsilon\kappa$, $\partial_r\theta_{\mathrm{b}}$ and $\partial_r\kappa$ as the other two approaches. Furthermore, $\partial_r\theta_{\mathrm{b}}$ is always zero. While this is obvious for Moore and Classic ($\theta_{\mathrm{b}}$ does not relate on $r$), this is not easily seen in the equations for model Twist. However, this result relies on the assumption, that all sensors have the same distance $r$ from the centerline resulting in a uniform "scaling" of the cross-section of the sensor array if $r$ varies. While $\partial_\varepsilon\kappa$ is zero at $\theta_{\mathrm{b}} = 90°$, the magnitude of $\partial_\varepsilon\theta_{\mathrm{b}}$ is maximal at this bending angle. More precisely, the position of those characteristic sensitivity values depends on the difference between of $\theta_{\mathrm{b}}$ and $\theta_i$. Because we chose $\theta_1 = 0$, they coincide with $\theta_{\mathrm{b}}$. Another value for $\theta_1$ (e.g. $\theta_1 = 30$) would shift them along the $\theta_{\mathrm{b}}$-axis accordingly. It can also been seen, that $\partial_\varepsilon\theta_{\mathrm{b}}$ decreases with bigger values of $\kappa$ and therefore with smaller bending radius. Furthermore, $\partial_\varepsilon\kappa$ is constant in $\kappa$, while $\partial_r\kappa$ is constant in $\theta_{\mathrm{b}}$.

For model Twist, sensitivities $\partial_\varepsilon|\varrho'|$ and $\partial_r|\varrho'|$ are mostly constant but also show several spikes. As we will discuss in the next paragraph, theses sensitivities are quite high at operational points with small values of $|\varrho'|$ as chosen for these

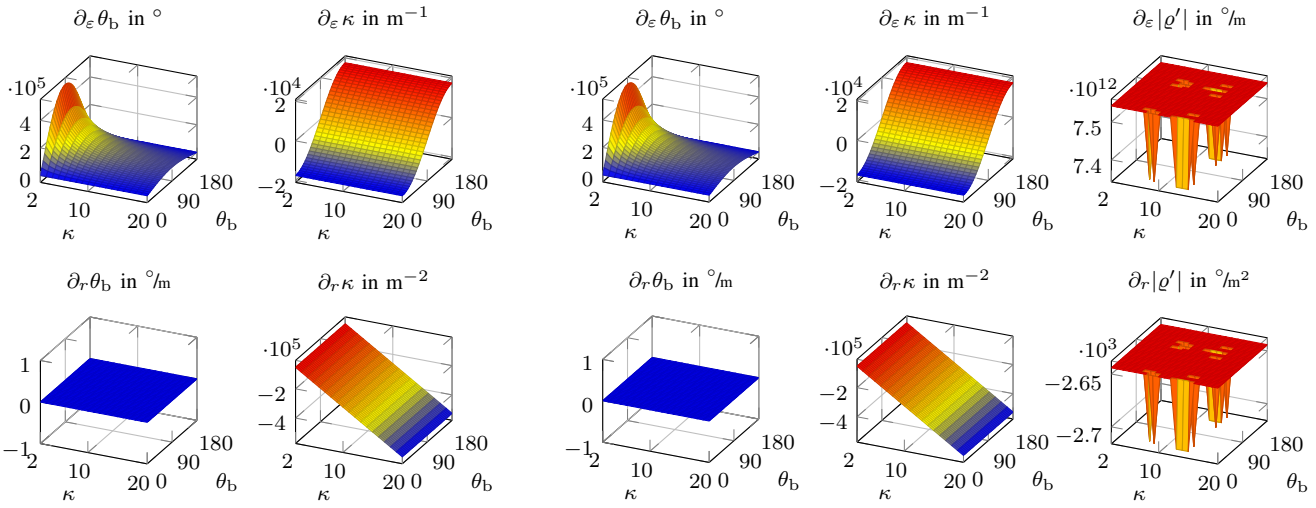


(a) model Moore and Classic (b) model Twist

Fig. 8. Sensitivity values for models Moore, Classic and Twist with $\boldsymbol{\varrho'}$ = 0.1 °/m and varying $\boldsymbol{\kappa}$ and $\boldsymbol{\theta_b}$. $\boldsymbol{\kappa}$ is given in $\mathbf{m^{-1}}$ and $\boldsymbol{\theta_b}$ in °.

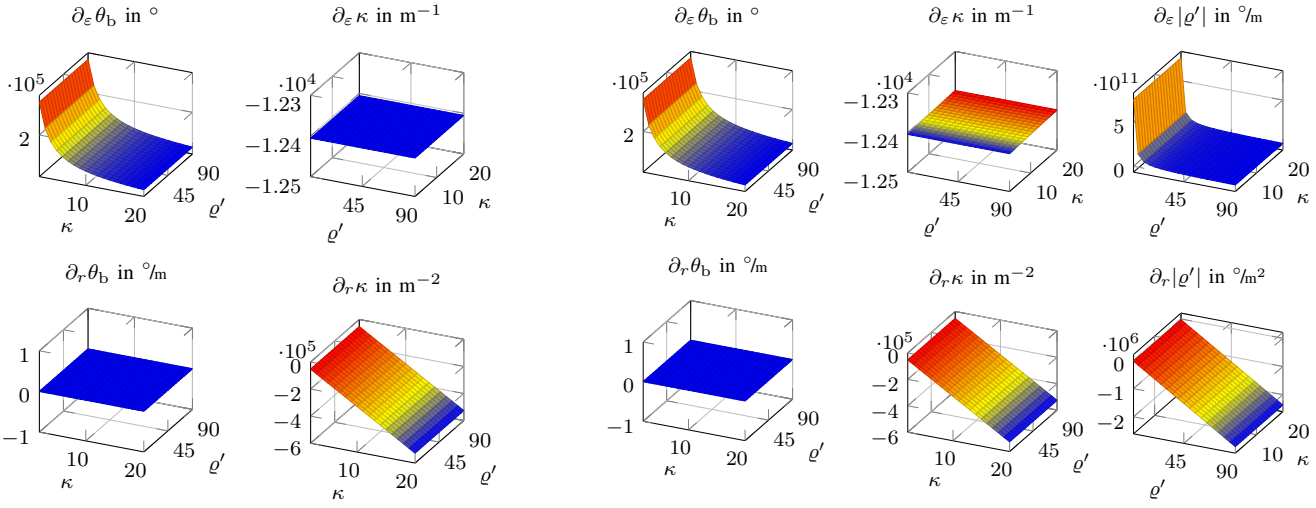


(a) model Moore and Classic (b) model Twist

Fig. 9. Sensitivity values for models Moore, Classic and Twist with $\boldsymbol{\theta_b}$=45° and varying $\boldsymbol{\kappa}$ and $\boldsymbol{\varrho'}$. $\boldsymbol{\kappa}$ is given in $\mathbf{m^{-1}}$ and $\boldsymbol{\varrho'}$ in °/m.

simulations. Therefore, even small numerical imprecisions during the calculation results in spiking results. Furthermore, the value of $\partial_\varepsilon |\varrho'|$ is quite high. Interrogators for FBGs have a wavelength accuracy of approximately 1 pm. Assuming a Bragg wavelength of 1500 nm, this results in a systematic strain error $\Delta\varepsilon$ of about $1 \cdot 10^{-6}$ and therefore a value for $\varrho'$ of about $7.54 \cdot 10^6$ °/m. Accumulated over the length of a sensing segment of 5 mm, this could result in an additional twisting error of about $37.7 \cdot 10^3$°. Hence, for a nearly untwisted sensor array, the twisting angle calculation in model Twist is quite sensitive to disturbances of strain measurements.

To evaluate the influence of $\varrho'$ on the sensitivity values, we vary $\varrho' \in [1\,°/\mathrm{m}, 90\,°/\mathrm{m}]$ and $\kappa \in [2\,\mathrm{m}^{-1}, 20\,\mathrm{m}^{-1}]$ while fixing $\theta_b$ at 45°. The results of this second set of simulations are shown in Fig. 9. Again, the sensitivities for models Moore and Classic are the same and are depicted in a single plots (see Fig. 9a). Also $\partial_\varepsilon \theta_b$, $\partial_r \theta_b$ and $\partial_r \kappa$ are similar between the three models as seen by comparing Fig. 9a and Fig. 9b. $\partial_\varepsilon \theta_b$, $\partial_\varepsilon \kappa$ and $\partial_r \kappa$ are always constant in $\varrho'$. There is a slight difference in $\partial_\varepsilon \kappa$ between the model Twist and the other two approaches. While for Moore and Classic this sensitivity is constant in $\kappa$, it is proportional to $\kappa$ for Twist (as indicated by the color gradient). However, compared to the average magnitude of $\partial_\varepsilon \kappa$, this slope is quite small ($0.333\,\mathrm{m}^{-1}/\mathrm{m}^{-1}$) and therefore, $\partial_\varepsilon \kappa$ can be seen as constant. Hence, $\varrho'$ does not influence $\partial_\varepsilon \theta_b$, $\partial_\varepsilon \kappa$, $\partial_r \theta_b$ and $\partial_r \kappa$. Furthermore, the sensitivity value $\partial_r |\varrho'|$ shows a linear relationship with $\varrho'$. The value for $\partial_\varepsilon |\varrho'|$ is high for small $\varrho'$, but decreases rapidly with increasing twist rate. This is coherent with the findings of the previous set of simulations. Therefore, especially for small twist rates $\varrho'$, it is important, that noise in the strain measurements is minimized. Otherwise, a significant error in the calculation of the twist rate of the sensor array's body frame occurs which reduces the accuracy of the shape reconstruction algorithm.

## V. Conclusion

In this paper, we derived an analytic model to calculate curve parameters based on longitudinal strain measurements of a bent, elongated, and twisted sensor array. Using differential geometry, we are able to reconstruct the centerline of the array. We developed our model in parallel but independently of Yi *et al.* [26]. In contrast to their work, we provide a closed-form solution for the curve parameters and also consider elongation. In contrast to other approaches found in the literature, utilizing a longitudinal sensor arrangement simplifies the production of the sensor system. Comparing our approach with two state-of-the-art models shows equivalent reconstruction accuracy in the untwisted case. However, our reconstruction algorithm shows significantly better accuracy if the sensor array is subject to twist. As a consequence of the coaxial alignment of the sensor array, the twist direction of the sensor array must be known in advance. In many cases, this information can be reasoned from knowledge about the environment. For example, in terms of continuum robotics, the twist direction of the robot can be estimated from its actuation values.

Because the curve parameters are calculated in closed-form, we are able to provide analytic equations for the model sensitivity which can be used in error propagation calculations. In the case of pure bending, sensitivities are similar to those of other state-of-the-art models. Nevertheless, if the sensor array is only slightly twisted, the twist rate calculated by our model shows a high sensitivity with respect to disturbances in strain measurements, which may lead to imprecise values. However, this sensitivity decreases rapidly with increasing twist rate.

Because our current model assumes constant temperature conditions, a further analysis will investigate the influence of temperature changes on the model and how these effects can be compensated. In addition, real-world experiments will be conducted to further validate our reconstruction algorithm. By applying it to measure the shape of twisted continuum robots, it promises an increased reconstruction accuracy which will be beneficial for whole-body closed-loop control. Furthermore, the proposed method can be applied easily to other applications outside the field of robotics, e.g. to reconstruct the shape of undersea cables or pipelines.

## Appendix I
## Sensitivity Values

Additionally to $\mathrm{s}_i$, $\mathrm{c}_i$ and $\mathrm{s}_{xy}$, we define $\mathrm{s_b} \coloneqq \sin(\theta_\mathrm{b})$, $\mathrm{c_b} \coloneqq \cos(\theta_\mathrm{b})$, $\mathrm{c}_{xy} \coloneqq \cos(\theta_x - \theta_y)$ and $\mathrm{c}_{x\mathrm{b}} \coloneqq \cos(\theta_x - \theta_\mathrm{b})$ Note, that $u, v \in \{1, 2, 3\}, u \neq v$ denote indices of the sensors in the sensing segment.

### A. *Model* Classic

$$\frac{\partial \theta_\mathrm{b}}{\partial \varepsilon_1} = \frac{B_1(H_2+H_3) - H_3(B_2-B_3)}{\varepsilon_1^2(H_1^2+B_1^2) + 2\varepsilon_1 K + (H_2+H_3)^2 + (B_2+B_3)^2}$$
$$\frac{\partial \theta_\mathrm{b}}{\partial r} = 0$$
$$\frac{\partial \kappa}{\partial \varepsilon_1} = \frac{\frac{\partial \theta_\mathrm{b}}{\partial \varepsilon_1} D_1 \left(D_3\,\mathrm{s_b} - D_2\,\mathrm{c_b}\right) + \frac{\partial D_1}{\partial \varepsilon_1}\left(D_2\,\mathrm{s_b} - D_3\,\mathrm{c_b}\right)}{\left(D_2\,\mathrm{s_b} + D_3\,\mathrm{c_b}\right)^2}$$
$$\frac{\partial \kappa}{\partial r} = \frac{1}{r^2}\frac{\varepsilon_u - \varepsilon_v}{\mathrm{s_b}(\mathrm{s}_u - \mathrm{s}_v) + \mathrm{c_b}(\mathrm{c}_u - \mathrm{c}_v)}$$

with

$$H_1 \coloneqq \mathrm{c}_2 - \mathrm{c}_3; \quad H_2 \coloneqq \varepsilon_2(\mathrm{c}_3 - \mathrm{c}_1); \quad H_3 \coloneqq \varepsilon_3(\mathrm{c}_1 - \mathrm{c}_2)$$
$$B_1 \coloneqq \mathrm{s}_2 - \mathrm{s}_3; \quad B_2 \coloneqq \varepsilon_2(\mathrm{s}_3 - \mathrm{s}_1); \quad B_3 \coloneqq \varepsilon_3(\mathrm{s}_1 - \mathrm{s}_2)$$
$$D_1 \coloneqq \frac{\varepsilon_v - \varepsilon_u}{r}; \quad D_2 \coloneqq \mathrm{s}_u - \mathrm{s}_v; \quad D_3 \coloneqq \mathrm{c}_u - \mathrm{c}_v$$

and

$$K \coloneqq H_1(H_2+H_3) + B_1(B_2+B_3)$$
$$\frac{\partial D_1}{\partial \varepsilon_1} = \begin{cases} -r^{-1} & \text{if } u = 1 \\ r^{-1} & \text{if } v = 1 \\ 0 & \text{otherwise} \end{cases}$$

Sensitivity values $\frac{\partial \varrho'}{\partial \varepsilon_i}$ and $\frac{\partial \varrho'}{\partial r}$ are not defined.

### B. *Model* Moore

$$\frac{\partial \theta_\mathrm{b}}{\partial \varepsilon_1} = \frac{\mathrm{s}_1(\varepsilon_2\,\mathrm{c}_2 + \varepsilon_3\,\mathrm{c}_3) - \mathrm{c}_1(\varepsilon_2\,\mathrm{s}_2 + \varepsilon_3\,\mathrm{s}_3)}{G}$$
$$\frac{\partial \theta_\mathrm{b}}{\partial r} = 0$$
$$\frac{\partial \kappa}{\partial \varepsilon_1} = \frac{2}{3r}\frac{\mathrm{c}_1(\varepsilon_2\,\mathrm{c}_2 + \varepsilon_3\,\mathrm{c}_3) + \mathrm{s}_1(\varepsilon_2\,\mathrm{s}_2 + \varepsilon_3\,\mathrm{s}_3) + \varepsilon_1}{\sqrt{G}}$$
$$\frac{\partial \kappa}{\partial r} = -\frac{2}{3r^2}\sqrt{G}$$

with $G \coloneqq \left(\sum_{i=1}^{3} \varepsilon_i\,\mathrm{c}_i\right)^2 + \left(\sum_{i=1}^{3} \varepsilon_i\,\mathrm{s}_i\right)^2$. Sensitivity values $\frac{\partial \varrho'}{\partial \varepsilon_i}$ and $\frac{\partial \varrho'}{\partial r}$ are not defined.

### C. *Model* Twist

$$\frac{\partial \theta_\mathrm{b}}{\partial \varepsilon_1} = \frac{\mathrm{s}_{uv}\left(A_v \frac{\partial A_u}{\partial \varepsilon_1} - A_u \frac{\partial A_v}{\partial \varepsilon_1}\right)}{A_u^2 + A_v^2 - 2A_uA_v\,\mathrm{c}_{uv}}$$
$$\frac{\partial \theta_\mathrm{b}}{\partial r} = \frac{\mathrm{s}_{uv}\left(A_v \frac{\partial A_u}{\partial r} - A_u \frac{\partial A_v}{\partial r}\right)}{A_u^2 + A_v^2 - 2A_uA_v\,\mathrm{c}_{uv}}$$
$$\frac{\partial \kappa}{\partial \varepsilon_1} = \frac{\frac{\partial \theta_\mathrm{b}}{\partial \varepsilon_1}\tan(\theta_i - \theta_\mathrm{b})(U_i - E_\mathrm{a})}{r\,\mathrm{c}_{i\mathrm{b}}} - \frac{E_i \frac{\partial E_i}{\partial \varepsilon_1} - r^2 \varrho' \frac{\partial \varrho'}{\partial \varepsilon_1}}{r\,\mathrm{c}_{i\mathrm{b}}\,U_i}$$
$$\frac{\partial \kappa}{\partial r} = \frac{\frac{\partial \theta_\mathrm{b}}{\partial r}\tan(\theta_i - \theta_\mathrm{b})}{r\,\mathrm{c}_{i\mathrm{b}}} + \frac{U_i - E_\mathrm{a}}{r^2\,\mathrm{c}_{i\mathrm{b}}} + \frac{r\varrho' \frac{\partial \varrho'}{\partial r} + \varrho'^2}{U_i\,\mathrm{c}_{i\mathrm{b}}}$$
$$\frac{\partial |\varrho'|}{\partial \varepsilon_1} = \frac{\delta_\mathrm{G} W \frac{\partial Q}{\partial \varepsilon_1}}{2r\sqrt{1-W^2}\sqrt{\left(\frac{E_\mathrm{a}}{2}\right)^2 - Q}}$$
$$\frac{\partial |\varrho'|}{\partial r} = -\frac{1}{r^2}\sqrt{1-W^2}$$

with

$$W = \frac{E_\mathrm{a}}{2} + \delta_\mathrm{G}\sqrt{\left(\frac{E_\mathrm{a}}{2}\right)^2 - Q}$$
$$\frac{\partial A_i}{\partial \varepsilon_1} = -\frac{1}{U_i}\left(r^2 \varrho' \frac{\partial \varrho'}{\partial \varepsilon_1} + E_i \frac{\partial E_i}{\partial \varepsilon_1}\right)$$
$$\frac{\partial A_i}{\partial r} = -\frac{r\varrho'}{U_i}\left(r\frac{\partial \varrho'}{\partial r} + \varrho'\right); \qquad U_i = \sqrt{E_i^2 - (r\varrho')^2}$$

## REFERENCES


[1] G. Robinson and J. Davies, "Continuum robots - a state of the art," in *IEEE International Conference on Robotics and Automation*, vol. 4, 1999, pp. 2849–2854.

[2] I. D. Walker, "Continuous Backbone "Continuum" Robot Manipulators," *ISRN Robotics*, vol. 2013, pp. 1–19, 2013.

[3] J. Burgner-Kahrs, D. C. Rucker, and H. Choset, "Continuum Robots for Medical Applications: A Survey," *IEEE Transactions on Robotics*, vol. 31, no. 6, pp. 1261–1280, 2015.

[4] X. Dong, D. Palmer, D. Axinte, and J. Kell, "In-situ repair/maintenance with a continuum robotic machine tool in confined space," *Journal of Manufacturing Processes*, vol. 38, no. December 2018, pp. 313–318, 2019.

[5] C. Shi, X. Luo, P. Qi, T. Li, S. Song, Z. Najdovski, T. Fukuda, and H. Ren, "Shape Sensing Techniques for Continuum Robots in Minimally Invasive Surgery: A Survey," *IEEE Transactions on Biomedical Engineering*, vol. 64, no. 8, pp. 1665–1678, 2017.

[6] X. Ma, P. W.-Y. Chiu, and Z. Li, "Real-Time Deformation Sensing for Flexible Manipulators With Bending and Twisting," *IEEE Sensors Journal*, vol. 18, no. 15, pp. 6412–6422, 2018.

[7] A. Vandini, C. Bergeles, B. Glocker, P. Giataganas, and G.-Z. Yang, "Unified Tracking and Shape Estimation for Concentric Tube Robots," *IEEE Transactions on Robotics*, vol. 33, no. 4, pp. 901–915, 2017.

[8] S. Song, Z. Li, M. Q. Meng, H. Yu, and H. Ren, "Real-Time Shape Estimation for Wire-Driven Flexible Robots With Multiple Bending Sections Based on Quadratic Bézier Curves," *IEEE Sensors Journal*, vol. 15, no. 11, pp. 6326–6334, 2015.

[9] H. Guo, F. Ju, Y. Cao, F. Qi, D. Bai, Y. Wang, and B. Chen, "Continuum robot shape estimation using permanent magnets and magnetic sensors," *Sensors and Actuators A: Physical*, vol. 285, pp. 519–530, 2019.

[10] J. P. Moore and M. D. Rogge, "Shape sensing using multi-core fiber optic cable and parametric curve solutions," *Optics Express*, vol. 20, no. 3, p. 2967, 2012.

[11] T. Lai, P. Cheng, C. Yan, C. Li, W. Hu, and M. Yang, "2D and 3D Shape Sensing Based on 7-Core Fiber Bragg Gratings," *Photonic Sensors*, no. November 2019, 2020.

[12] X. Yi, J. Qian, L. Shen, Y. Zhang, and Z. Zhang, "An Innovative 3D Colonoscope Shape Sensing Sensor Based on FBG Sensor Array," in *International Conference on Information Acquisition*. IEEE, 2007, pp. 227–232.

[13] R. J. Roesthuis and S. Misra, "Steering of Multisegment Continuum Manipulators Using Rigid-Link Modeling and FBG-Based Shape Sensing," *IEEE Transactions on Robotics*, vol. 32, no. 2, pp. 372–382, 2016.

[14] Q. Qiao, D. Willems, G. Borghesan, M. Ourak, J. De Schutter, and E. V. Poorten, "Estimating and Localizing External Forces Applied on Flexible Instruments by Shape Sensing," in *International Conference on Advanced Robotics*. IEEE, 2019, pp. 227–233.

[15] F. Khan, A. Denasi, D. Barrera, J. Madrigal, S. Sales, and S. Misra, "Multi-Core Optical Fibers With Bragg Gratings as Shape Sensor for Flexible Medical Instruments," *IEEE Sensors Journal*, vol. 19, no. 14, pp. 5878–5884, 2019.

[16] S. Sefati, R. Hegeman, F. Alambeigi, I. Iordachita, and M. Armand, "FBG-Based Position Estimation of Highly Deformable Continuum Manipulators: Model-Dependent vs. Data-Driven Approaches," in *International Symposium on Medical Robotics*. IEEE, 2019, pp. 1–6.

[17] D. C. Rucker and R. J. Webster III, "Statics and Dynamics of Continuum Robots With General Tendon Routing and External Loading," *IEEE Transactions on Robotics*, vol. 27, no. 6, pp. 1033–1044, 2011.

[18] J. Starke, E. Amanov, M. T. Chikhaoui, and J. Burgner-Kahrs, "On the merits of helical tendon routing in continuum robots," in *IEEE/RSJ International Conference on Intelligent Robots and Systems*. IEEE, 2017, pp. 6470–6476.

[19] J. Wei, S. Wang, J. Li, and S. Zuo, "Novel Integrated Helical Design of Single Optic Fiber for Shape Sensing of Flexible Robot," *IEEE Sensors Journal*, vol. 17, no. 20, pp. 6627–6636, 2017.

[20] K. C. Galloway, Y. Chen, E. Templeton, B. Rife, I. S. Godage, and E. J. Barth, "Fiber Optic Shape Sensing for Soft Robotics," *Soft Robotics*, vol. 6, no. 5, pp. 671–684, 2019.

[21] S. Lim and S. Han, "Shape estimation of a bent and twisted cylinder using strain from a sensor array in triple helices," *Measurement Science and Technology*, vol. 29, no. 9, p. 095003, 2018.

[22] R. Xu, A. Yurkewich, and R. V. Patel, "Curvature, Torsion, and Force Sensing in Continuum Robots Using Helically Wrapped FBG Sensors," *IEEE Robotics and Automation Letters*, vol. 1, no. 2, pp. 1052–1059, 2016.

[23] M. Chadha and M. D. Todd, "A comprehensive kinematic model of single-manifold Cosserat beam structures with application to a finite strain measurement model for strain gauges," *International Journal of Solids and Structures*, vol. 159, pp. 58–76, 2019.

[24] M. Chadha and M. D. Todd, "An Improved Shape Reconstruction Methodology for Long Rod Like Structures Using Cosserat Kinematics-Including the Poisson's Effect," in *Nonlinear Dynamics, Conference Proceedings of the Society for Experimental Mechanics Series*, G. Kerschen, Ed., 2019, vol. 1, pp. 237–246.

[25] Q. Guo, Z. Li, Q. Liu, and H. Wang, "Twist Angle Compensation for Three Dimensional Real-Time Shape Sensing Method Based on Multi-Core Optical Fiber," in *International Conference on Measuring Technology and Mechatronics Automation*. IEEE, 2020, pp. 402–406.

[26] X. Yi, X. Chen, H. Fan, F. Shi, X. Cheng, and J. Qian, "Separation method of bending and torsion in shape sensing based on FBG sensors array," *Optics Express*, vol. 28, no. 7, p. 9367, 2020.

[27] R. L. Bishop, "There is More than One Way to Frame a Curve," *The American Mathematical Monthly*, vol. 82, no. 3, pp. 246–251, 1975.

[28] J. Langer and D. A. Singer, "Lagrangian Aspects of the Kirchhoff Elastic Rod," *SIAM Review*, vol. 38, no. 4, pp. 605–618, 1996.

[29] R. C. Allil, F. V. de Nazaré, and M. M. M. Werneck, *Fiber Bragg Gratings: Theory, Fabrication, and Applications*. SPIE, 2017.

[30] S. S. Antman, *Nonlinear Problems of Elasticity*, ser. Applied Mathematical Sciences. New York: Springer-Verlag, 2005, vol. 107.

[31] I. Floris, S. Sales, P. A. Calderón, and J. M. Adam, "Measurement uncertainty of multicore optical fiber sensors used to sense curvature and bending direction," *Measurement*, vol. 132, pp. 35–46, 2019.

[32] M. Grabe, *Measurement Uncertainties in Science and Technology*. Springer International Publishing, 2014.


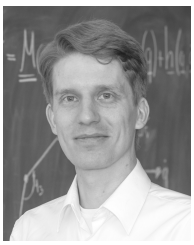

**Vincent Modes** received his Diplom degree in mechatronics from Dresden University of Technology (TUD), Germany in 2012.

After working as a software developer at KUKA Roboter GmbH, Augsburg he joined the Leibniz University Hannover, Germany where he is currently pursuing the Ph.D. degree at the Institute of Mechatronic Systems. His research interest is focused on continuum robots, including calibration, shape sensing and control.

**Tobias Ortmaier** studied electrical engineering at the Technische Universität München and received his diploma in 1998 and his PhD in 2003, respectively.

From 1998 until 2003 he was a research assistant at the "Institute of Robotics and Mechatronics" of the German Aerospace Center (DLR), Oberpfaffenhofen, Germany working on minimally invasive robotic surgery and associated technologies. From 2003 until 2004 he joined the "Laboratoire de Robotique de Paris", Université de Paris 6 (Pierre et Marie Curie), France as post doc and returned to the DLR thereafter. From 2006 until 2008 he worked as project manager at KUKA Roboter GmbH, Augsburg, Germany being responsible for medical robotic and robotic surgery development projects. Since October 2008, he has been full professor at the "Institute of Mechatronic Systems" (imes) at the Leibniz Universität Hannover, Hanover, Germany. Besides research in robotics and mechatronics he is very active in the field of technology transfer and spin-offs.

**Jessica Burgner-Kahrs** (M'08, S'18) received the Diplom and Ph.D. degrees in computer science from Karlsruhe Institute of Technology (KIT), Germany in 2006 and 2010 respectively.

She is currently an Associate Professor with the Departments for Mathematical & Computational Sciences, Computer Science, and Mechanical & Industrial Engineering, the founding Director of the Continuum Robotics Laboratory, and Associate Director of the Robotics Institute at the University of Toronto, Canada. Her research focus lies on continuum robotics and in particular on their design, modelling, planning and control, as well as human-robot interaction. Her fundamental robotics research is driven by applications in minimally-invasive surgery and maintenance, repair, and operations.